A Parametric UWB Propagation Channel Estimation and Its Performance Validation in an Anechoic Chamber

Katsuyuki Haneda, *Student Member, IEEE*, Jun-ichi Takada, *Member, IEEE*, and Takehiko Kobayashi, *Member, IEEE*

***Abstract*—This paper presents an ultrawide-band (UWB) channel sounding scheme with a parametric channel estimation to seek accurate probing of the propagation channel. The channel sounder consists of a vector network analzer and synthetic array to measure spatial transfer functions. The measured data are then applied to a maximum-likelihood (ML)-based estimator. The concepts implemented in the ML-based parametric channel estimation are: 1) to probe frequency-dependent effects in magnitude and phase of propagation paths and 2) to incorporate with robust concept of direction finding, namely, the spherical wavefront model of incident waves. The whole frequency band was divided into subbands, and the estimation of magnitude and phase was conducted in each subband. The spherical wavefront model includes a new model parameter, curvature radii, which is not covered in the conventional plane wavefront model. Performances of the proposed parametric UWB channel estimation scheme was assessed by anechoic chamber tests. The test demonstrated that: 1) the frequency-dependent magnitude and phase were accurately detected if the path was resolved and 2) the spherical wavefront outperformed the plane wavefront to model measured data given the short-range environment. Furthermore, fundamental performance of the sounding scheme, i.e., angular and time resolutions, were also evaluated in the test.**

***Index Terms*—Parametric channel estimation, spherical wavefront model, ultrawide-band (UWB) communication, UWB propagation.**

I. INTRODUCTION

DEMANDS FOR wireless communications with indoor applications have been emerging, such as those for wireless local-area and sensor networks. Indoor environments often reveal rich multipath propagation due to dense scattering objects, which are illuminated by mobile or fixed terminals. From the propagation measurement and modeling point of view, dense multipaths are difficult to treat accurately. One possible solution to the problem is to introduce an ultrawide-band (UWB) signal that offers fine time resolution. This paper presents the introduction of UWB signals for channel sounding, with the objective of performing a precise and accurate investigation of indoor propagation channels.

Thus far, several channel sounding systems have been proposed and developed, e.g., [1]–[7], all of which are for wide-band sounding in the frequency domain. Among them, the sounder described by Thomä *et al.* [1] has recently been expanded to operate UWB signals [8]. In contrast, among the available papers which report UWB channel sounding and modeling results [9]–[18], only [12]–[14] presented results from parametric channel estimation in the time domain.

The UWB channel sounding we propose is based on the conventional wide-band sounding schemes, in which the design is done in the frequency domain. The sounding can be achieved with simply configured equipment, as used by Suzuki and Mohan [7]. A vector network analyzer (VNA) and a single-element antenna with a spatial scanner, which conforms to a synthetic aperture, are widely used structures to measure the spatial distribution of transfer functions. Furthermore, we considered the model-based characterization of the measured transfer functions. In particular, we assume that the UWB channels can be expressed as a set of propagation paths, and then we find the model parameters of each path, such as direction-of-arrival and delay time, to best fit the measured data. The scheme is thus called parametric channel estimation. Maximum-likelihood (ML)-based criterion was introduced to find the model parameters of paths. Conventionally the ML-based criterion is applied for the wide-band channel modeling [4], but it can be modified to treat UWB signals [19]. Our proposed UWB channel sounding and parametric channel estimation have strength that have not yet been addressed in most papers, which are: 1) to investigate frequency-dependent effects of magnitude and phase in propagation paths and 2) to incorporate the robust wavefront model of incident paths into the parametric UWB channel estimation.

The frequency-dependent effects of magnitude and phase in propagation paths occur due to path loss, antenna directivities, and power loss in reflection, diffraction, and penetration. These frequency-dependent effects cannot be ignored in UWB bands. Our channel modeling approach treats the whole UWB band as a concatenation of several subbands and probes the frequency-dependent magnitude and phase in each subband.

As to the robust wavefront model, we will introduce the spherical wavefront [20], [21]. When estimating the directional information using antenna arrays, wavefronts of incident paths have to be determined beforehand. A plane wavefront is widely used, but it assumes that the sources are infinitely away from

---

Manuscript received July 27, 2005; revised January 14, 2006.

K. Haneda and J. Takada are with the UWB Technology Institute, National Institute of the Information and Communications Technology, Kanagawa 239-8047, Japan and also with the Tokyo Institute of Technology, Tokyo 152-8550, Japan (e-mail: haneda@ap.ide.titech.ac.jp; takada@ide.titech.ac.jp).

T. Kobayashi is with the UWB Technology Institute, National Institute of the Information and Communications Technology, Kanagawa 239-8047, Japan and also with the Department of Information and Communication Engineering, Tokyo Denki University, Tokyo 101-8457, Japan (e-mail: koba@c.dendai.ac.jp).

Digital Object Identifier 10.1109/TMTT.2006.871990

the arrays. This model is not realistic in indoor environments where many scattering objects are placed close to the antenna arrays. On the contrary, the spherical wavefront model can characterize the sources with finite length from the array, so improvement of the model-based estimation is expected.

Finally, to verify the newly proposed aspects in UWB channel sounding and parametric channel estimation algorithm, we conducted anechoic chamber tests [21].

This paper is organized as follows. Section II defines the UWB path model for the parametric channel estimation. Then, we formulate a cost function to find model parameters based on the ML criterion. A subband expression of UWB signals and the spherical wavefront model were incorporated in the formulation. Section III covers an experiment performed in an anechoic chamber to evaluate the effectiveness of the proposed approach. Finally, Section IV summarizes this paper.

II. PARAMETRIC CHANNEL ESTIMATION IN UWB CHANNEL SOUNDING

Parametric channel estimation requires a certain model to fit the measured data. This section describes a UWB path model used for the UWB parametric channel estimation and formulates a cost function to determine the model parameters based on the ML criterion.

A. UWB Path Model

Let us assume UWB communications exploit high-frequency bands in which the electromagnetic propagation behaviors can be characterized by ray-path models yielded by the Fermat's Principle, e.g., [22]. We can then define that one propagation path has direction-of-departure (DOD) $\mathbf{\Omega}^{\mathrm{Tx}}$, direction-of-arrival (DOA) $\mathbf{\Omega}^{\mathrm{Rx}}$, and delay time τ, which do not depend on frequency and polarization and has a frequency-dependent polarimetric gain. Assuming that only a single T_x antenna element is excited, we can define $D_V^{\mathrm{Tx}}(f, \mathbf{\Omega}^{\mathrm{Tx}})$ and $D_H^{\mathrm{Tx}}(f, \mathbf{\Omega}^{\mathrm{Tx}})$ as radiation patterns expressed by complex amplitude for vertical and horizontal polarizations, respectively. On the receiving antenna side, $D_V^{\mathrm{Rx}}(f, \mathbf{\Omega}^{\mathrm{Rx}})$ and $D_H^{\mathrm{Rx}}(f, \mathbf{\Omega}^{\mathrm{Rx}})$ are defined as radiation patterns for a single antenna element for each polarization. The radio channel consists of antennas at link ends and propagation, and its transfer function is a multiplication of transfer functions of T_x and R_x antennas and propagation. Using the notations defined above, the transfer function $s(f)$ of the radio channel is expressed as follows in the equivalent baseband form:

$$s(f) = \alpha(f, \tau) \begin{bmatrix} D_V^{\mathrm{Rx}}(f, \mathbf{\Omega}^{\mathrm{Rx}}) \\ D_H^{\mathrm{Rx}}(f, \mathbf{\Omega}^{\mathrm{Rx}}) \end{bmatrix}^H \cdot \begin{bmatrix} r_{VV}(f) & r_{VH}(f) \\ r_{HV}(f) & r_{HH}(f) \end{bmatrix} \begin{bmatrix} D_V^{\mathrm{Tx}}(f, \mathbf{\Omega}^{\mathrm{Tx}}) \\ D_H^{\mathrm{Tx}}(f, \mathbf{\Omega}^{\mathrm{Tx}}) \end{bmatrix} \quad (1)$$

where $\cdot^H$ denotes an Hermitian transpose operation, $\alpha(f, \tau)$ and $r(f)$ represent the transfer function during propagation, and $\alpha(f, \tau)$ is a complex gain in free space denoted by

$$\alpha(f, \tau) = \frac{1}{4\pi f \tau} \exp(-\mathrm{j}2\pi f \tau). \quad (2)$$

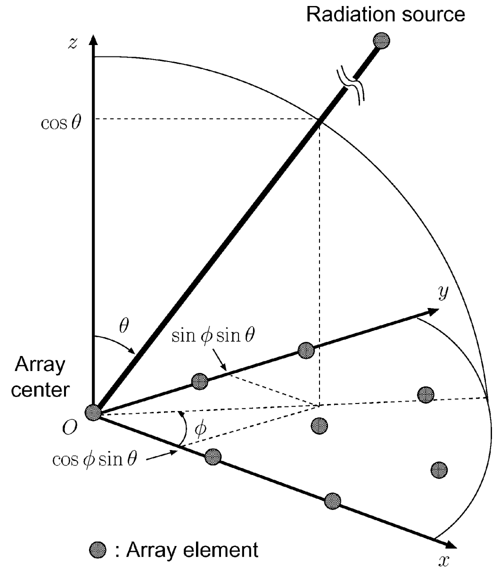

Fig. 1. Definition of the coordinate system in the considered model.

Equation (2) is the Friis' transmission formula [23] for complex amplitude which assumes a constant gain of the receiving antennas. The matrix with elements $r(f)$ expresses scattering loss from reflection, diffraction, and penetration in complex amplitude. The diagonal elements denote scattering coefficients for copolarization, while the nondiagonals represent a polarization rotation effect.

B. Subband Model

As the antenna directivity and propagation loss including scattering loss and free space path loss does not drastically change within a limited bandwidth, we can divide the whole band into I subbands, and $s(f)$ within the band can be modeled as constant. The ith subband have center frequency $f_{\mathrm{c}i}$, bandwidth of B, and constant transfer function s_i.

C. Wavefront Models

Wavefront is an aperture consisting of a constant phase in wave propagation for a single wave. It is necessary to assume a wavefront model of incident paths to estimate its directional information at link ends using array antennas. The wavefront model determines the phase differences between antenna elements of the array. As the phase difference contains directional information, we can extract directional information by measuring the phase differences. Here, we will introduce two wavefront models, i.e., spherical and plane wave models.

The spherical wave model [20] can be expressed mathematically by using azimuthal and polar angles ϕ and θ and the curvature radius from a source point to the array center R. The coordinate system is defined in Fig. 1. A position vector from the array center to the source point $\mathbf{r}_{\mathrm{source}}(\mathbf{\Omega}_{\mathrm{sp}})$ is expressed as

$$\mathbf{r}_{\mathrm{source}}(\mathbf{\Omega}) = [R\cos\phi\sin\theta \quad R\sin\phi\sin\theta \quad R\cos\theta]^T$$

where $\mathbf{\Omega}_{\mathrm{sp}} = [\phi, \theta, R]$ and $\cdot^T$ denotes a transpose operation. A position vector of each antenna element $\mathbf{r}_{\mathrm{array}}$ is expressed as

$$\mathbf{r}_{\mathrm{array}} = [d_x \quad d_y \quad d_z]^T$$

where d_x, d_y, and d_z denote the distance from the array center to the antenna elements on x, y, and z coordinates, respectively. The phase difference between the array center and kth antenna element ψ_k can be derived by the difference of distances between source to array center and source to kth antenna element. As the distance from source to array center is R and that from source to the kth antenna element is $\|\mathbf{r}_{\mathrm{source}} - \mathbf{r}_{\mathrm{array},k}\|$, the resulting phase difference yields

$$\psi_k(f, \mathbf{\Omega}) = \frac{2\pi f}{c}\left(\|\mathbf{r}_{\mathrm{source}} - \mathbf{r}_{\mathrm{array},k}\| - R\right). \tag{3}$$

In case of the plane wavefront model, the dimension of $\mathbf{\Omega}$ is reduced to two, namely, $\mathbf{\Omega}_{\mathrm{pl}} = [\phi, \theta]$. The phase difference can be obtained for the plane wavefront model as in

$$\psi_k(f, \mathbf{\Omega}) = \frac{2\pi f}{c}\langle \mathbf{r}_{\mathrm{plane}}, \mathbf{r}_{\mathrm{array},k}\rangle \tag{4}$$

where $\langle\cdot\rangle$ denotes an operation of inner product and $\mathbf{r}_{\mathrm{plane}}$ corresponds to the directional cosines of a unit vector

$$\mathbf{r}_{\mathrm{plane}}(\mathbf{\Omega}_{\mathrm{pl}}) = [\cos\phi\sin\theta \quad \sin\phi\sin\theta \quad \cos\theta]^T. \tag{5}$$

It should be noted that the plane wavefront is equivalent to the spherical wavefront with infinite curvature radii. As the model order of the spherical wavefront model is one dimension larger than that of the plane wavefront model due to the curvature radii, the spherical wavefront model has the potential to characterize physical phenomena more precisely than the plane wavefront model does.

If we assume that L waves are propagating from element k_1 of the T_x array to element k_2 of the R_x array, then the transfer function observed at frequency f_{k_3} within the ith subband, $H_{k_1k_2k_3,i}$ can be expressed as

$$\begin{aligned} H_{k_1k_2k_3,i} &= \sum_{l=1}^{L} s_{l,i} \exp\left\{-\mathrm{j}\psi_{k_1,l}^{\mathrm{Tx}}\left(f_{k_3,i}\right)\right\} \\ &\quad \cdot \exp\left\{-\mathrm{j}\psi_{k_2,l}^{\mathrm{Rx}}\left(f_{k_3,i}\right)\right\} \exp\left(-\mathrm{j}2\pi f_{k_3,i}\tau_l\right) \\ &\equiv \sum_{l=1}^{L} h_{l,k_1k_2k_3,i}. \end{aligned} \tag{6}$$

In this paper, we call $s_{l,i}$ the reference transfer function of the lth wave in the ith subband. It is called "reference" because it expresses the transfer function between the array centers of the T_x and R_x. It must be noted that simultaneous DOD and DOA estimation with the spherical wavefront model is impossible, because the spherical wavefront model assumes a radiation from point sources, which contradicts the use of an array on both sides of the link, as depicted in Fig. 2.

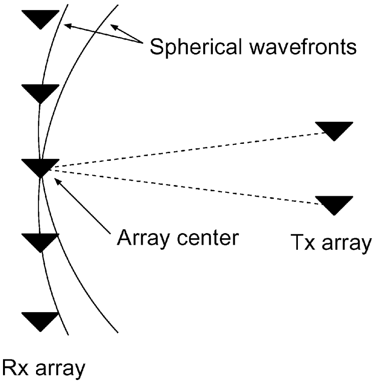

Fig. 2. Spherical wavefront model is incompatible with simultaneous DOD and DOA estimation: different radiation sources in the T_x array result in different shapes for spherical wavefronts in the R_x array.

D. ML-Based Estimator for UWB Signals

ML estimation is a procedure that finds a set of parameters that maximizes the likelihood function. The likelihood function in our case is the conditional probability of measured data, given a model of signal components, its model parameters, and probability density functions (pdfs) of the noise. The signal model and its parameters were defined in the previous subsections. The noise component is assumed to follow the identically and independently distributed (i.i.d.) complex Gaussian distribution, where its mean and power are equal to 0 and σ^2, respectively.

Let us first define the notation of several quantities. The measured data in experiments are composed of the transfer functions perturbed by thermal noise $n_{k_1k_2k_3,i}$ as

$$\begin{aligned} y_{k_1k_2k_3,i} &= H_{k_1k_2k_3,i} + n_{k_1k_2k_3,i} \\ &= \sum_{l=1}^{L} h_{l,k_1k_2k_3,i} + n_{k_1k_2k_3,i}. \end{aligned}$$

To simplify the notations, we vectorize the set of data obtained by array measurements into

$$\mathbf{y} = \mathbf{H} + \mathbf{n} = \sum_{l=1}^{L} \mathbf{h}_l + \mathbf{n} \in C^{KI} \tag{7}$$

where K represents total number of measured data in the ith subband. In addition, we define a model parameter set $\boldsymbol{\mu}$ as

$$\boldsymbol{\mu} = \left[\{s_{l,i}\}_i, \mathbf{\Omega}_l^{\mathrm{Tx}}, \mathbf{\Omega}_l^{\mathrm{Rx}}, \tau_l\right]_{l=1}^{L}. \tag{8}$$

Using the notations defined above, the likelihood function is expressed as

$$p(\mathbf{y}|\boldsymbol{\mu}) = \prod_{k_1,k_2,k_3,i}\left[\frac{1}{\pi\sigma}\cdot\exp\left(-\frac{\left|y_{k_1k_2k_3,i} - H_{k_1k_2k_3,i}\right|^2}{\sigma^2}\right)\right]. \tag{9}$$

By taking the logarithm of (9), the log-likelihood function is simplified as follows:

$$\log\left[p(\mathbf{y}|\boldsymbol{\mu})\right] = -KI\log\pi\sigma - \frac{\|\mathbf{y}-\mathbf{H}(\boldsymbol{\mu})\|^2}{\sigma^2}. \quad (10)$$

Thus, the ML estimation of parameters which maximize the likelihood function in (9) is

$$\hat{\boldsymbol{\mu}} = \arg\max_{\boldsymbol{\mu}} p(\mathbf{y}|\boldsymbol{\mu}) = \arg\min_{\boldsymbol{\mu}} \|\mathbf{y}-\mathbf{H}(\boldsymbol{\mu})\|^2 \quad (11)$$

where $\hat{\cdot}$ means that the parameter is estimated. Finding $\boldsymbol{\mu}$ in (11) is computationally prohibitive due to the large simultaneous search dimensions. Here, we introduce the expectation and maximization (EM) algorithm [24] to reduce the simultaneous search dimension. The EM algorithm first estimates the transfer function of each path $\mathbf{x}_l$ from the measured data $\mathbf{y}$ as

$$\mathbf{x}_l = \mathbf{h}_l + \beta_l(\mathbf{y}-\mathbf{H}) \quad (12)$$

where β_l has a constraint

$$\sum_{l=1}^{L}\beta_l = 1, \quad \beta_l > 0, \qquad \text{for all } l. \quad (13)$$

Equation (12) means that the expected value of the noise for each path is expressed as a part of the measured noise component. Practically, $\beta = 1/L$ for all l, which maximizes the conditional Fisher information of the estimated $\mathbf{x}_l$ [14]. The log-likelihood function for $\mathbf{x}_l$ is analogous to (11) as

$$\hat{\boldsymbol{\mu}}_l = \arg\min_{\boldsymbol{\mu}_l} \|\mathbf{x}_l - \mathbf{h}_l(\boldsymbol{\mu}_l)\|^2 \quad (14)$$

where $\boldsymbol{\mu}_l$ is a set of model parameters for the lth wave

$$\boldsymbol{\mu}_l = \left[\{s_{l,i}\}_i, \boldsymbol{\Omega}_l^{\mathrm{Tx}}, \boldsymbol{\Omega}_l^{\mathrm{Rx}}, \tau_l\right]. \quad (15)$$

Equation (14) corresponds to the maximization step of the EM algorithm. The simultaneous search dimension is reduced compared to (9) as a result of dividing the whole data into each path.

Here, we define the array steering vector of the lth wave for the ith subband $\mathbf{a}_{l,i} \in C^K$. The steering vector composed of the phase difference entries with respect to the phase center in an array outputs

$$a_{l,k_1k_2k_3,i} = \exp\left\{-\mathrm{j}\psi_{k_1,l}^{\mathrm{Tx}}(f_{k_3,i})\right\}\exp\left\{-\mathrm{j}\psi_{k_2,l}^{\mathrm{Rx}}(f_{k_3,i})\right\} \cdot \exp\left(-\mathrm{j}2\pi f_{k_3,i}\tau_l\right). \quad (16)$$

Using the array steering vector, (14) can be rewritten as

$$\hat{\boldsymbol{\mu}}_l = \arg\min_{\boldsymbol{\mu}_l} \sum_{i=1}^{I} \|\mathbf{x}_{l,i} - s_{l,i}\mathbf{a}_{l,i}(\boldsymbol{\mu}_l')\|^2 \quad (17)$$

where $\mathbf{x}_{l,i}$ is the estimated data of the lth path in the ith subband and

$$\boldsymbol{\mu}_l' = \left[\boldsymbol{\Omega}_l^{\mathrm{Tx}}, \boldsymbol{\Omega}_l^{\mathrm{Rx}}, \tau_l\right]. \quad (18)$$

Equation (17) is a procedure that finds the model parameters $\boldsymbol{\mu}_l'$ which extract the largest power from $\mathbf{x}_l$. Thus, we can reorganize the procedure by a matched filter approximation

$$\hat{\boldsymbol{\mu}}_l' = \arg\max_{\boldsymbol{\mu}_l'} \sum_{i=1}^{I} \left\|\mathbf{a}_{l,i}^H(\boldsymbol{\mu}_l')\mathbf{x}_{l,i}\right\|^2. \quad (19)$$

The maximization procedure can be reduced to one-dimensional (1-D) sequential search using the space-alternating generalized EM (SAGE) algorithm [25]. The search is conducted parameter by parameter, iteratively updating the parameters. During a search of one parameter, other parameters are kept fixed. As it is verified that the log-likelihood function is monotonically increasing in the sequential search, an iteration of the set of sequential search can reach a certain maximum value of the log-likelihood function.

After $\boldsymbol{\mu}_l$ is estimated, the reference transfer functions $s_{l,i}$ can then be obtained by utilizing a part of the likelihood function within the ith subband. It is derived as a maximum value of the matched filter output

$$\hat{s}_{l,i} = \frac{\mathbf{a}_{l,i}^H(\hat{\boldsymbol{\mu}}_l')\mathbf{x}_{l,i}}{\mathbf{a}_{l,i}^H(\hat{\boldsymbol{\mu}}_l')\mathbf{a}_{l,i}(\hat{\boldsymbol{\mu}}_l')} \quad (20)$$

where the ith subband spans the frequency band between $(f_{\mathrm{c}i} - B/2)$ and $(f_{\mathrm{c}i} + B/2)$. $\hat{\boldsymbol{\mu}}_l'$ denotes an estimated result of model parameters which is common over the whole frequency band. Here, if we assume that the reference transfer function of each subband is represented by that at the center frequency of the subband, we can derive the reference transfer function at any frequency from (20) by shifting the subband, namely, shifting the center frequency, with a constant B. This scheme is used to estimate reference transfer functions in anechoic chamber tests, as we will describe in Section III.

E. Succesive Interference Cancellation (SIC)-Type Implementation of the ML-Based Estimator

We implemented the ML-based estimator in an SIC manner [26]. Although the main drawback of the SIC-type path detection is error propagation, the fine time resolution offered by UWB signals can mitigate it, since the detection and removal of the paths are conducted in an accurate manner. The SIC-type procedure is equivalent to the EM algorithm with the number of paths equals to one and consists of the following steps.

Step 1) Find a value of model parameter of the strongest path, given the measured data $\mathbf{y}$ substituting into (19).

Step 2) Find the reference transfer function $\hat{s}_i$ using the estimated model parameter and (20).

Step 3) Reconstruct data of the strongest path $\mathbf{h}$ using (6) and remove it from the original data $\mathbf{y}$.

Step 4) Substitute the resultant data $(\mathbf{y}-\mathbf{h})$ into $\mathbf{y}$, and return to step 1).

Step 5) Continue the set of steps mentioned above until the number of paths reaches a predefined number or power of the detected path is below a certain threshould level, e.g., the noise level.

In finding a value of model parameters in Step 1), a combination of a coarse global mesh search based on the EM algorithm and a fine local search based on the SAGE algorithm was employed. In the coarse global mesh search, we find the region which may include the values of parameters that give the maximum value of the log-likelihood function. After the region is specified, a fine local search is conducted inside the region to find the value of parameters accurately.

F. Consideration of Subbands

The bandwidth for subband B can be optimized under the SIC-based implementation of the ML-based estimator. Let us assume that the two paths are $\Delta\psi$ and $\Delta\tau$ apart in the azimuthal and delay domains, respectively. Furthemore, we define Ξ_ψ and Ξ_τ as a Fourier resolution of the estimator in the azimuthal and delay domains. The fourier resolution in the azimuthal and delay domains refer to the 3-dB beamwidth of the beampattern spanned by antenna arrays and the value of the fraction of measurement bandwidth, respectively. In fact, the selection of the value of the subband indicates a tradeoff between accurate estimation of the reference transfer functions and achievable time resolution. The larger the bandwidth that is dedicated to achieve greater time resolution, the larger the error in the results of the estimated reference transfer functions. Therefore, the following criteria are recommended in selecting the optimum value of the subbands.

1) When $\Delta\psi > \Xi_\psi$:
   As the path is already resolved in the angular domain, the use of a narrower bandwidth is recommended where variations in antennas and propagation characteristics are reasonably small, in order to probe frequency-dependent magnitude and phase accurately.
2) When $\Delta\psi < \Xi_\psi$:
   The value of B should be more than a fraction of the value $\Delta\tau$ to resolve two paths in the delay domain.

The criteria are summarized in Fig. 3.

III. PERFORMANCE ASSESSMENT OF THE PROPOSED APPROACH

To asesss the performance of the proposed UWB channel sounding scheme and subsequent parametric channel estimation, we conducted measurements in an anechoic chamber. In particular, the objectives of the measurement are: 1) to assess the angular and time resolution; 2) to confirm the detection of frequency-dependent magnitude and phase in path loss; and 3) to evaluate the plane and spherical wavefront models and compare their results. The data were collected with the measurement system depicted in Fig. 4. The system consisted of a VNA and a synthetic array on the R_x side. Two sources were realized on the T_x side by introducing a 3-dB power divider in assessing resolution. The relative position of the sources were arbitrarily configured. DOA of the sources was estimated on the R_x side. The other specifications for the anechoic chamber tests are listed in Table I. The antennas used in the tests were UWB monopole antennas [28] whose characteristics were known prior to the experiment. Radiation patterns on the azimuthal plane are available in complex values. Fluctuation of the group delay is less than 0.1 ns within the measurement bandwidth. The antennas radiate vertical polarization, so the reference transfer function (1) is approximately reduced as in (21) by substituting $D_H^{\mathrm{Rx}}(f,\mathbf{\Omega}^{\mathrm{Rx}}) = 0$ and $D_H^{\mathrm{Tx}}(f,\mathbf{\Omega}^{\mathrm{Tx}}) = 0$ to yield

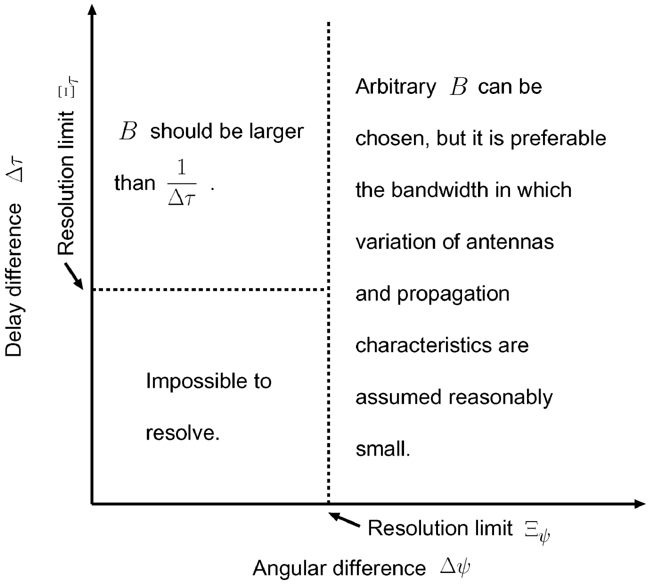

Fig. 3. Appropriate subband B for separation of two paths which have $\Delta\psi$ and $\Delta\tau$ difference in angular and delay domains, respectively.

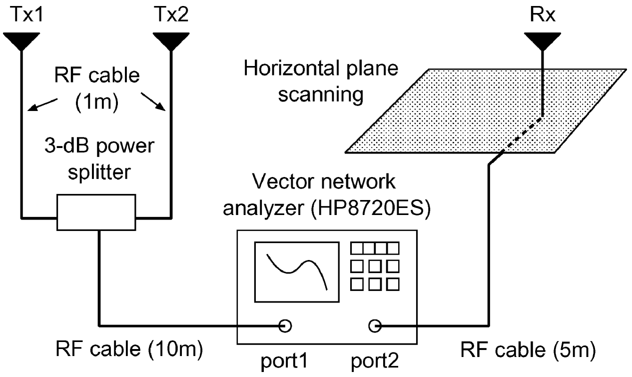

Fig. 4. UWB spatio-temporal channel measurement system.

$$s(f) = \alpha(f,\tau) D_V^{\mathrm{Rx}}(f,\mathbf{\Omega}^{\mathrm{Rx}}) r_{VV}(f) D_V^{\mathrm{Tx}}(f,\mathbf{\Omega}^{\mathrm{Tx}}). \tag{21}$$

As back-to-back calibration was done, the impedance mismatch effects between the cables and antennas were negligible. In the following sections, all of the results presented are after the removal of the antenna directivities. To remove the antenna directivities: 1) the DOA was estimated for each path from the measurements; 2) the DOD was calculated for each path after the measurements by using the antenna positions in the test scenarios; 3) the complex antenna transfer function was determined for the T_x and R_x antennas using the DOD and DOA information; and finally 4) the reference transfer function of paths

TABLE I
SPECIFICATIONS FOR ANECHOIC CHAMBER TESTS

Bandwidth	3.1 to 10.6 GHz [27].
Frequency sweeping points	801.
Spatial sampling	10×10 points in horizontal plane. Element spacing is 48 mm, which is less than half the wavelength at 3.1 GHz.
Estimated components	DOA azimuth, polar angles, curvature radius, delay time, and magnitude and phase of the reference transfer function.
Antennas	UWB monopole antennas [28].
Polarization	Vertical–vertical.
SNR at receiver	About 25 dB.
Calibration	Internal function of the VNA, Back-to-back, the distance between Tx and Rx is 5.0 m.

TABLE II
PARAMETERS ESTIMATED IN THE ANGULAR RESOLUTION TEST. THEORETICAL VALUES ARE SHOWN IN PARENTHESES

	Azimuth [deg]	Polar [deg]	Delay [ns]	Curvature radius [m]
#1	0.40	87.70	16.67	5.30
	(0.00)	(86.57)	(16.70)	(5.01)
#2	10.20	88.90	16.67	4.95
	(10.00)	(86.57)	(16.70)	(5.01)

TABLE III
PARAMETERS ESTIMATED IN THE TIME-RESOLUTION TEST. THEORETICAL VALUES ARE SHOWN IN PARENTHESES

	Azimuth [deg]	Polar [deg]	Delay [ns]	Curvature radius [m]
#1	0.30	87.90	16.00	4.75
	(0.00)	(86.42)	(16.03)	(4.81)
#2	0.30	88.80	16.67	5.10
	(0.00)	(86.57)	(16.70)	(5.01)

obtained in the measurements were divided by the complex antenna gains, and only the propagation characteristics remain.

A. Evaluation of Angular Resolution

The element spacing of the synthetic array was 48 mm in the angular resolution test, which was equivalent to 0.49λ at the lowest frequency of the measurement. However, the element spacing was larger than half the wavelength in the higher frequency region, which did not fulfill the sampling theorem in the spatial domain. This results in an aliasing in the angular domain, but it cannot be a problem when the log-likelihood function is calculated with all of the frequency-domain data. As a result, angular resolution is restricted by the lowest frequency, because a constant physical aperture length corresponds to a smaller electrical aperture in the lower frequency region, ending up with a wider beamwidth and lower angular resolution. As the electrical aperture length of the synthetic array was 4.5λ at the lowest frequency, this corresponded to approximately 7° in the 3-dB beamwidth, which could be regarded as the inherent angular resolution of the array.

In the test, two paths with the same delay times and polar angles, but with 10° of difference in the incident azimuthal angle of arrival were investigated for accuracy in resolution and detection. Eight hundred megahertz was chosen for the subband, but almost the same results were obtained for an arbitrary bandwidth for the subbands. We assumed the spherical wavefront model to estimate the angles. The estimated parameters for the two paths are listed in Table II. The theoretical values are also listed in parenthesis, which were calculated from the T_x and R_x positions in the scenario. In Fig. 5, we can see the estimated reference transfer functions and theoretical values for each path. The theoretical characteristics were calculated from Friis' transmission formula described in (2). The estimated magnitude and phase of the spectrum agreed well with the theoretical characteristics. These results proved that the approach could achieve an angular resolution that is close to the Fourier resolution.

B. Evaluation of Time Resolution

Since the measurement system used the 7.5-GHz bandwidth, inherent Fourier resolution in the delay domain was 0.13 ns, which is equivalent to 4 cm. However, in the time-resolution tests, two different paths 0.67 ns (20 cm) apart were examined because the size of antennas prevented us from placing the antennas closer than that distance and to avoid electrical coupling of the two sources. Following the criteria in Fig. 3, the value of bandwidth for the subband B was selected as a fraction of the delay time difference, i.e., $1/\Delta\tau = 1.5$ GHz. The results for estimating the parameters and spectrum are listed in Table III and Fig. 6, respectively. The results revealed that the two paths were accurately separated, while spectrum extraction partly failed in the highest and lowest frequency regions. This is due to the limited bandwidth of the measurement. As we stated before, estimation of the reference transfer function at a certain frequency f_{ci} requires log-likelihood function spanned in bandwidth $(f_{ci} - B/2) \leq f_{ci} \leq (f_{ci} + B/2)$. However, it is obvious that a sufficient bandwidth of subband B to resolve two paths is not assured if f_{ci} is within the highest and lowest frequency regions of $f_{\min} \leq f_{ci} < (f_{\min} + B/2)$ and $(f_{\max} - B/2) < f_{ci} \leq f_{\max}$, respectively. $f_{\min}$ and $f_{\max}$ denote the lowest and highest frquencies of the measurement frequency band. In the experimental results, the bandwidth where spectrum estimation was incorrect was $B/2 = 0.75$ and 1.2 GHz for the first and second detected paths, respectively. The wider bandwidth in the second path was due to overestimating the power for detecting the first path in the lowest and highest frequency regions. Furthermore, we conducted additional time-resolution tests with $\Delta\tau$ varied from 0.67 to 2.00 ns, i.e., from 20 to 60 cm, and determined the bandwidth B_I where spectrum estimation failed. The result is shown in Fig. 7. The results indicated that the first detected path closely agreed with $B_I = 1/2\Delta\tau$, while those for the second path indicated larger values than for the first paths, but smaller than $B_I = 1/\Delta\tau$.

C. Robustness of Wavefront Models

It is often the case in indoor scenarios that spherical incidence of paths seems more realistic than with the plane wavefront model. However, even if complicated signal models are used, there is always signal model error. The more the signal model deviates from the physical propagation phenomena, the more significant the errors are in estimating model parameters.

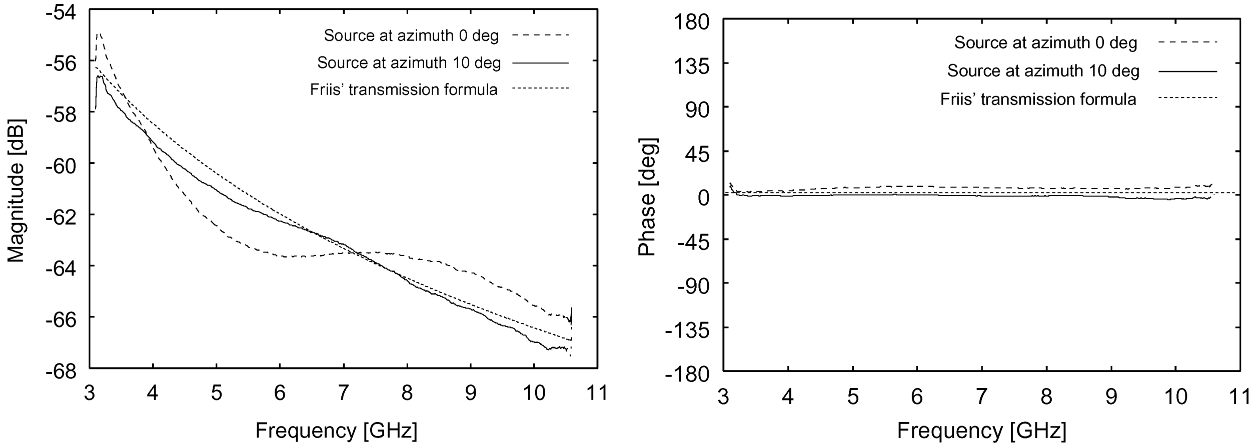

(a) (b)

Fig. 5. Results of estimating spectrum in the angular resolution test: two paths with the same delay times, but 10° difference in DOA azimuthal angles. (a) Magnitude. (b) Phase components.

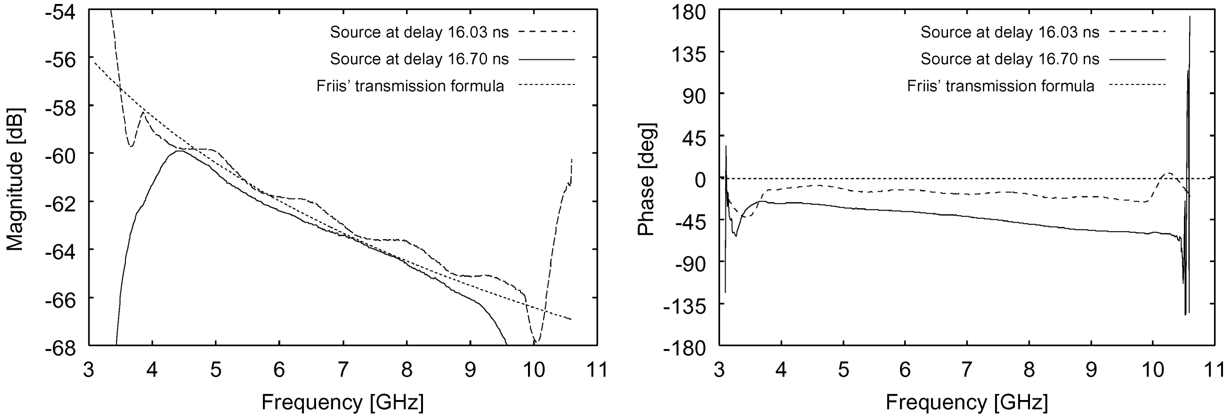

(a) (b)

Fig. 6. Result of estimating parameters in the time resolution test: two paths with the same DOAs, but different delay time of 0.67 ns. (a) Magnitude. (b) Phase components.

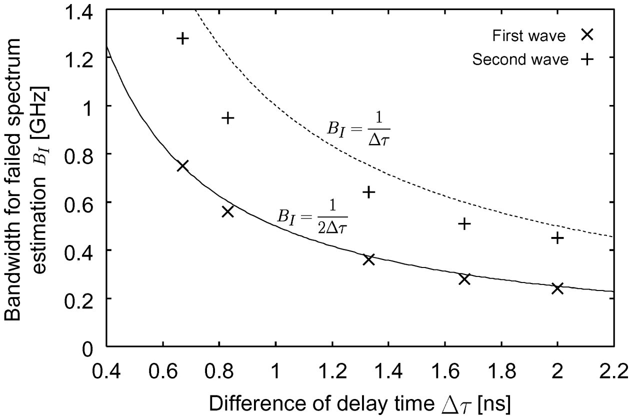

Fig. 7. Relation between difference in delay time and bandwidth in which spectrum estimation fails.

Specifically, the error appears as a spurious path, which cannot be identified in real environments. The spurious paths often prevent us from accurately detecting weaker paths, making it difficult to investigate the physical phenomena correctly.

Here, we will present one example that estimates paths incident from azimuth 0° (#1) and 15° (#2). Plane and spherical wavefront models were assumed in estimating the angles, and their performance was evaluated and compared. Note that the power for source #2 was 20 dB weaker than that for point source #1, using the attenuator for source #2. After the stronger path #1 was successfully detected and removed, the log-likelihood function was calculated to detect source #2. Fig. 8 plots the results of the calculation using both wavefront models. The peak appeared in the direction of the true source with the spherical wavefront model, while the plane wavefront model failed to detect the source #2, due to its larger response at ±5°, which seemed to be residual components of source #1. In this case, the parametric channel estimator regards the peak at 5° as the second strongest source, resulting in the production of a spurious path. Spurious paths were detected even for the third path, and, finally, the true source was detected in the fourth detection. This indicates that the spherical wavefront model expresses the physical propagation phenomena more precisely.

The robustness of the spherical wavefront model can also be evaluated with respect to the residual power after paths are de-

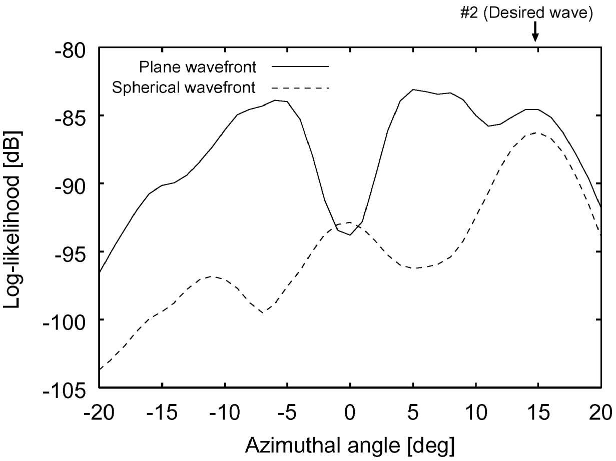

Fig. 8. Log-likelihood spectrum in the angle domain for the detection of source #2 (weaker source).

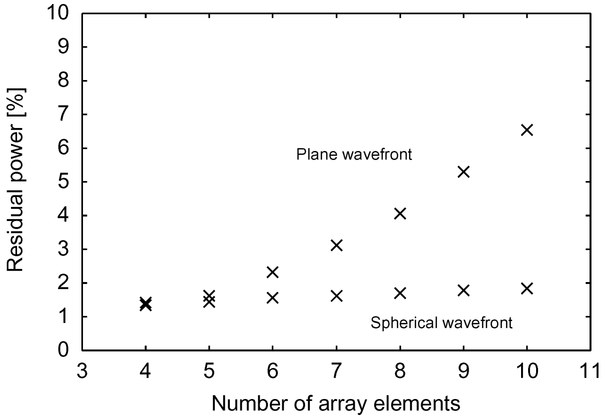

Fig. 9. Results from detection of single path in anechoic chamber. Residual power after detecting a path is plotted for the plane and spherical wavefront models.

tected and extracted. If the residual power is limited, this indicates that the signal model fits the measured data well. In contrast, greater amounts of residual power mean greater deviations in the signal model. We detected a single path by using an antenna array with several aperture sizes in the anechoic chamber tests. Both spherical and plane wavefront models were used as signal models, and residual power after the extraction of the path was evaluated. The results are plotted in Fig. 9. We can see that the spherical wavefront model always accomplishes less residual power, regardless of the size of the array. Furthermore, the residual power increases monotonically as the array size increases, indicating that a larger array results in larger signal model deviations from the measured data.

It is again worth mentioning that the plane wavefront is considered to be part of the spherical wavefront, since they are equivalent as curvature radii of the spherical model approaches infinity. However, estimating large curvature radii may result in large errors, due to the small gradient of the log-likelihood function. In iteratively calculating the log-likelihood in the ML-based estimator, a small gradient often results in more iterations until convergence to stationary points, which is burdensome in terms of calculations. We must also bear in mind that the accurate results yielded by the spherical wavefront model are achieved at the expense of increasing the computational burden.

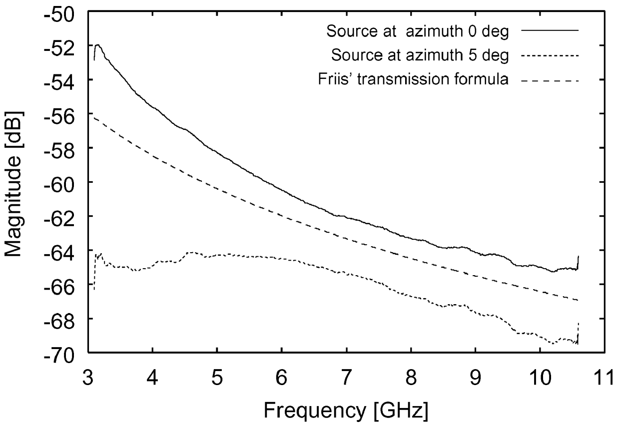

Fig. 10. Estimated spectrum of two paths which have closer spatial characteristics than the inherent Fourier angular resolution and no delay difference.

D. Other Considerations

1) Resolving Two Paths Which are Closer Than the Inherent Fourier Resolution: It is a matter of interest how the algorithm behaves in the detection of two incident paths, which are closer in the angular-delay domain than the inherent Fourier resolution. For example, the results of estimating the spectrum for two paths, which have 5° different azimuthal incidences but no delay or polar differences, are plotted in Fig. 10. As the angular difference was less than the inherent Fourier resolution, the spectrum for the second path was underestimated, as a consequence of overestimating the power for the first path. However, angle and delay parameters were accurately estimated. Note that a multidimensional spatio-temporal channel estimation will offer much higher resolution than the single-dimensional estimation. This is one of the advantages of using multidimensional channel estimation.

2) Accuracy of Estimation in Endfire Direction: Employing a horizontal synthetic array on the R_x side, paths may be incident from the endfire direction of the array. The endfire direction refers to the direction where the effective size of antenna aperture is minimum, resulting in a lowest capability to resolve paths and estimate parameters accurately due to the wide beamwidth. In the case of horizontal array, polar angle around 90° corresponds to the endfire direction. In fact, the results of anechoic chamber tests revealed deviating estimates of polar angles from theoretical values due to the endfire incidence of paths. Here, Monte Carlo simulation was conducted to evaluate the rms error of the estimated parameters by assuming path incidence from endfire direction. In the simulations, azimuthal angle, curvature radius, and delay time were randomly assigned for each path. Incident paths were assumed to be resolved correctly, i.e., with 10° or 0.67-ns differences in the azimuthal and delay domains with each other. The signal-to-noise ratio was 20 dB at a center frequency 6.85 GHz. The rms error we obtained is plotted in Fig. 11. We can see that the large polar angles, i.e., incidence of paths from endfire direction, resulted in large errors of estimation in the polar angles to an extent of 1°. The rms error was

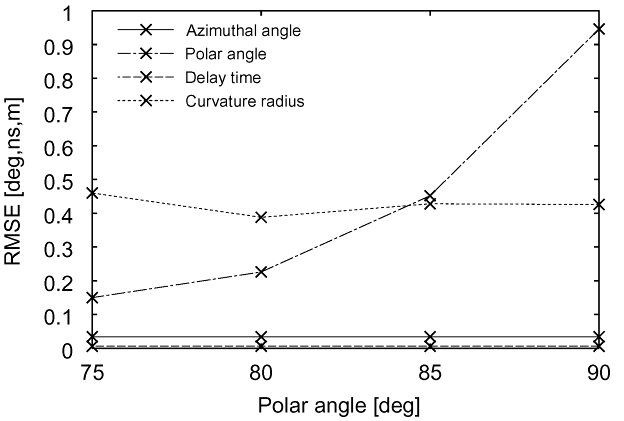

Fig. 11. RMS error of the estimated parameters. Paths are incident to endfire direction of array.

also remarkable in the curvature radius, regardless of the other parameter sets that are estimated. This is attributed to the small gradient in the log-likelihood function with respect to variations in the curvature radius, as we pointed out previously.

IV. SUMMARY AND CONCLUSION

This paper has presented the UWB channel sounding scheme with a parametric channel estimation based on the ML criterion. Having conducted the anechoic chamber tests to assess the performances of the proposed approach: 1) angular and time resolution of the sounding system approaches the inherent Fourier resolution of the measurement which are determined by the size of antenna aperture and signal bandwidths; 2) frequency-dependent magnitude and phase in path loss is accurately detected as long as paths were resolved; and 3) the spherical wavefront model can outperform the plane wavefront model given the short-range environment of the anechoic chamber. Using this sounding scheme, several measurement campaigns in indoor scenarios have been carried out [29]–[31]. The results offered a closer look at propagation phenomena that sometime achieves the detection of "a single wave." The capability of the proposed channel sounding system and its results shall be dedicated to the accurate channel modeling activities, such as in [17],[18], and [32].

However, at the same time, it must be noted that the spherical wavefront model is still not sufficient to model the real physical phenomena properly. Even a simple diffraction yielded by the uniform theory of diffraction (e.g., [22]) cannot be exaclty modeled as spherical wavefronts. Another example that our approach cannot treat is Bragg scattering (e.g., [33]). It produces a scattering toward different directions depending on the frequency, which is actually observed in an experiment that measured a scattered wave from metal blinds of windows in indoor scenarios [34]. Scattering from a surface which has a roughness with the same dimension as the wavelength of the UWB signal is also an important issue to be analyzed in detail and modeled[35], [36]. The physical phenomena represented by the items above should be taken into consideration for further improvements in parametric channel estimation and modeling.

ACKNOWLEDGMENT

The authors would like to thank members of the NICT UWB Consortium, namely, Dr. A. Akeyama, Prof. K. Araki, F. Ohkubo, Dr. O. Sasaki, Dr. H. Zhang, I. Nishiyama, T. Miyamoto, Dr. M. Yoshikawa, and Dr. Y. Rikuta, for their great help in the experiment and fruitful discussions. The authors also would like to express great gratitude to the anonymous reviewers for their invaluable comments and suggestions to improve this paper.

REFERENCES

[1] R. S. Thomä, D. Hampicke, A. Richter, G. Somerkorn, A. Schneider, U. Trautwein, and W. Wirnitzer, "Identification of time-variant directional mobile radio channels," *IEEE Trans. Instrum. Meas.*, vol. 49, no. 2, pp. 357–364, Apr. 2000.

[2] T. Zwick, D. Hampicke, A. Richter, G. Sommerkorn, R. S. Thomä, and W. Wiesbeck, "A novel antenna concept for double-directional channel measurements," *IEEE Trans. Veh. Technol.*, vol. 53, no. 2, pp. 527–537, Feb. 2004.

[3] K. Kalliola, H. Laitinen, L. I. Vaskelainen, and P. Vainikainen, "Real-time 3D spatial–temporal dual-polarized measurement of wideband radio channel at mobile station," *IEEE Trans. Instrum. Meas.*, vol. 49, no. 2, pp. 439–448, Apr. 2000.

[4] B. H. Fleury, M. Tschudin, R. Heddergott, D. Dahlhaus, and K. I. Pedersen, "Channel parameter estimation in mobile radio environments using the SAGE algorithm," *IEEE J. Sel. Areas Commun.*, vol. 17, no. 3, pp. 434–449, Mar. 1999.

[5] K. Sakaguchi, J. Takada, and K. Araki, "A novel architecture for MIMO spatio–temporal channel sounder," *IEICE Trans. Electron.*, vol. E85-C, no. 3, pp. 436–441, Mar. 2002.

[6] R. D. Tingley and K. Pahlavan, "Space–time measurement of indoor radio propagation," *IEEE Trans. Instrum. Meas.*, vol. 50, no. 1, pp. 22–31, Feb. 2001.

[7] H. Suzuki and A. S. Mohan, "Measurement and prediction of high spatial resolution indoor radio channel characteristic map," *IEEE Trans. Veh. Technol.*, vol. 49, no. 4, pp. 1321–1333, Jul. 2000.

[8] R. Zetik, R. Thomä, and J. Sachs, "Ultra-wideband real-time channel sounder design and application," presented at the URSI Int. Electromagn. Theory Symp., Pisa, Italy, May 2004.

[9] A. A. M. Saleh and R. A. Valenzuela, "A statistical model for indoor multipath propagation," *IEEE J. Sel. Areas Commun.*, vol. SAC-5, no. 2, pp. 128–137, Feb. 1987.

[10] J. Kunisch and J. Pamp, "An ultra-wideband space-variant multipath indoor radio channel model," in *Proc. IEEE Ultra Wideband Syst. Technol. Conf.*, Reston, VA, Nov. 2003, pp. 290–294.

[11] Q. H. Spencer, B. D. Jeffs, M. A. Jensen, and A. L. Swindlehurst, "Modeling the statistical time and angle of arrival characteristics of an indoor multipath channel," *IEEE J. Sel. Areas Commun.*, vol. 18, no. 3, pp. 347–359, Mar. 2000.

[12] R. J. Cramer, R. A. Scholtz, and M. Z. Win, "Evaluation of an ultra-wide-band propagation channel," *IEEE Trans. Antennas Propag.*, vol. 50, no. 5, pp. 561–570, May 2002.

[13] M. Z. Win and R. A. Scholtz, "Characterization of ultra-wide bandwidth wireless indoor channels: A communication-theoretic view," *IEEE J. Sel. Areas Commun.*, vol. 20, no. 9, pp. 1613–1627, Dec. 2002.

[14] A. S. Y. Poon and M. Ho, "Indoor multiple antenna channel characterization from 2 to 8 GHz," presented at the IEEE Int. Commun. Conf., Anchorage, AK, May 2003, GC27-3.

[15] J. Karedal, S. Wyne, P. Almers, F. Tufvesson, and A. F. Molisch, "UWB channel measurements in an industrial environment," in *Proc. IEEE Global Telecommun. Conf.*, Dallas, TX, Nov. 2004, vol. 6, pp. 3511–3516.

[16] D. Cassioli, M. Z. Win, and A. F. Molisch, "The ultra-wide bandwidth indoor channel: from statistical model to simulations," *IEEE J. Sel. Areas Commun.*, vol. 20, no. 5, pp. 1247–1257, Aug. 2002.

[17] J. Foerster *et al.*, Channel modeling sub-committee report (final) IEEE P802.15-02/490r1-SG3a, Feb. 2003.

[18] A. F. Molisch *et al.*, IEEE 802.15.4a channel model—Final report IEEE P802.15-04/662r0-SG4a, Nov. 2004.

[19] K. Haneda and J. Takada, "An application of SAGE algorithm for UWB propagation channel estimation," in *Proc. IEEE Ultra Wideband Syst. Technol. Conf.*, Reston, VA, Nov. 2003, pp. 483–487.

[20] A. Ohmae, M. Takahashi, and T. Uno, Localization of sources in the finite distance using MUSIC algorithm by the spherical mode vector IEICE, Tokyo, Japan, Tech. Rep. AP2003-64/SAT2003-56/MW2003-70/OPE2003-57, Jul. 2003.
[21] K. Haneda, J. Takada, and T. Kobayashi, "Experimental evaluation of a SAGE algorithm for ultra wideband channel sounding in an anechoic chamber," in *Proc. Int. Ultra Wideband Syst. Joint Conf. Ultra Wideband Syst. Technol. Workshop*, Kyoto, Japan, May 2004, pp. 66–70.
[22] L. B. Felsen and N. Marcuvitz*, Radiation and Scattering of Waves*. Piscataway, NJ: IEEE Press, 1994.
[23] H. T. Friis, "A note on a simple transmission formula," *Proc. IRE*, vol. 34, no. 5, pp. 254–256, May 1946.
[24] A. P. Dempster, N. M. Laird, and D. B. Rubin, "Maximum likelihood from incomplete data via the EM algorithm," *J. Royal Statist. Soc. B*, vol. 39, no. 1, pp. 1–38, 1977.
[25] J. A. Fessler and A. O. Hero, "Space-alternating generalized expectation maximization algorithm," *IEEE Trans. Signal Process.*, vol. 42, no. 10, pp. 2664–2677, Oct. 1994.
[26] B. H. Fleury, X. Yin, K. G. Rohbrandt, P. Jourdan, and A. Stucki, "Performance of a high-resolution scheme for joint estimation of delay and bidirection dispersion in the radio channel," in *Proc. IEEE 55th Veh. Technol. Conf.*, May 2002, pp. 522–526.
[27] FCC, Revision of part 15 of the Commission's rules regarding ultra-wideband transmission systems FCC 02-48, Apr. 2002, First Rep. and Order.
[28] T. Taniguchi and T. Kobayashi, "An omni-directional and low-VSWR antenna for the FCC-approved UWB frequency band," in *Proc. IEEE AP-S Int. Symp.*, Jun. 2003, pp. 460–463.
[29] J. Takada, K. Haneda, and H. Tsuchiya, "Joint DOA/DOD/DTOA estimation system for UWB double directional channel modeling," in *Advances in Direction of Arrival Estimation*, S. Chandran, Ed. Norwell, MA: Artech House, 2006, ch. 17.
[30] K. Haneda, J. Takada, and T. Kobayashi, "Double directional ultra wideband channel characterization in a line-of-sight home environment," *IEICE Trans. Fundamentals*, vol. EA-88, no. 9, pp. 2264–2271, Sept. 2005.
[31] J. Takada, F. Ohkubo, K. Haneda, and T. Kobayashi, "Double directional ultra wideband propagation measurements in office environments," in *Proc. Int. Ultrawideband Conf.*, Zurich, Switzerland, Sep. 2005, pp. 16–20.
[32] L. Correia, Ed*., Toward Mobile Broadband Multimedia Networks—COST 273; European Co-Operation in Mobile Radio Research*. Oxford, U.K.: Elsevier, 2006.
[33] M. Born and E. Wolf, "Scattering from inhomogeneous media," in *Principles of Optics*. Cambridge, U.K.: Cambridge Univ. Press, 2001, ch. 13, pp. 705–708.
[34] H. Tsuchiya, N. Lertsirisopon, M. Ghoraishi, J. Takada, and T. Kobayashi, "Investigation of the Bragg scattering of UWB signal from the window blind (2): Experimental investigation," presented at the IEICE Gen. Conf., Mar. 2006.
[35] P. Pongsilamanee and H. L. Bertoni, "Specular and nonspecular scattering from building facades," *IEEE Trans. Antennas Propag.*, vol. 52, no. 7, pp. 1879–1889, Jul. 2004.
[36] H. Budiarto, K. Haneda, and J. Takada, "Prediction model for the estimation of nonspecular wave scattering characteristics on building surfaces," in *Proc. Int.. Antennas Propag. Symp*, Sendai, Japan, Aug. 2004, pp. 749–752.

Katsuyuki Haneda (S'03) was born in Yokohama, Kanagawa, Japan, in 1979. He received the B.E. and M.E. degrees from the Tokyo Institute of Technology, Tokyo, Japan, in 2002 and 2004, respectively.

His current interests are radio propagation measurements and modeling, array signal processing, UWB radio, and multiple-input multiple-output systems. He is currently a Research Fellow with the Japan Society for the Promotion of Science, Tokyo, Japan.

Mr. Haneda was the recipient of the Student Paper Award presented at the 7th International Symposium on Wireless Personal Multimedia Communications (WPMC '04). He is a student member of the Institute of Electronic, Information and Communication Engineers (IEICE), Japan.

Jun-ichi Takada (S'89–M'89) was born in Tokyo, Japan, in 1964. He received the B.E., M.E., and D.E. degrees from the Tokyo Institute of Technology, Tokyo, Japan, in 1987, 1989, and 1992, respectively.

From 1992 to 1994, he was a Research Associate Professor with Chiba University, Chiba, Japan. Since 1994, he has been an Associate Professor with the Tokyo Institute of Technology. His current interests are wireless propagation and channel modeling, array signal processing, UWB radio, software-defined radio, and applied radio instrumentation and measurements.

Dr. Takada is a member of the Institute of Electronic, Information and Communication Engineers (IEICE), Japan, ACES, and the ECTI Association Thailand. He has been an active member of European Cooperation in the field of Scientific and Technical research (COST) action 273 "Toward mobile broadband multimedia networks." He was the recipient of the 1993 IEICE Excellent Paper Award and the 1994 IEICE Young Engineer Award.

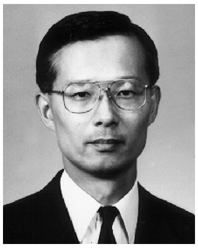

Takehiko Kobayashi (M'86) received the B.E., M.E., and Ph.D. degrees in electrical engineering from the University of Tokyo, Tokyo, Japan, in 1978, 1980, and 1983, respectively.

In 1983, he joined Nippon Telegraph and Telephone, where he was engaged in research on various wireless communication systems. In 1986, he was a Guest Scientist with the National Bureau of Standard [(now the National Insitute of Standards and Technology (NIST)], Boulder, CO. From 1998 to 2001, he was with YRP Key Tech Laboratories, where he focused on fourth-generation mobile communication systems. He is currently a Professor with the Department of Information and Communication Engineering, Tokyo Denki University, Tokyo, Japan. His current research interests include UWB wireless systems, mobile communication channel characterization, and teletraffic evaluation of mobile communication networks.

Dr. Kobayashi was the recipient of the Institute of Electronic, Communication and Information Engineers (IEICE), Japan, Best Paper Awards in 2001 and 2002 and the Telecom System Awards from the Telecommunications Advancement Foundation in 2003 and 2005.